Simulation of Atmospheric Visibility Impairment

Lin Zhang, *Senior Member, IEEE*, Anqi Zhu, Shiyu Zhao, and Yicong Zhou, *Senior Member, IEEE*

***Abstract*— Changes in aerosol composition and its proportions can cause changes in atmospheric visibility. Vision systems deployed outdoors must take into account the negative effects brought by visibility impairment. In order to develop vision algorithms that can adapt to low atmospheric visibility conditions, a large-scale dataset containing pairs of clear images and their visibility-impaired versions (along with other annotations if necessary) is usually indispensable. However, it is almost impossible to collect large amounts of such image pairs in a real physical environment. A natural and reasonable solution is to use virtual simulation technologies, which is also the focus of this paper. In this paper, we first deeply analyze the limitations and irrationalities of the existing work specializing on simulation of atmospheric visibility impairment. We point out that many simulation schemes actually even violate the assumptions of the Koschmieder's law. Second, more importantly, based on a thorough investigation of the relevant studies in the field of atmospheric science, we present simulation strategies for five most commonly encountered visibility impairment phenomena, including mist, fog, natural haze, smog, and Asian dust. Our work establishes a direct link between the fields of atmospheric science and computer vision. In addition, as a byproduct, with the proposed simulation schemes, a large-scale synthetic dataset is established, comprising 40,000 clear source images and their 800,000 visibility-impaired versions. To make our work reproducible, source codes and the dataset have been released at https://cslinzhang.github.io/AVID/.**

***Index Terms*— Atmospheric visibility impairment, atmospheric science, image simulation, synthetic datasets.**

I. Introduction

IN RECENT years, more and more imaging sensors and the accompanying vision systems have been being widely used for outdoor applications, such as surveillance [1], remote sensing [2], auto-driving vehicles [3], etc. While these sensors and algorithms are continuously getter better, they are mainly designed to operate well on clear weather conditions. Researchers are beginning to notice that vision systems deployed outdoors must consider the adverse effects of atmospheric visibility impairment. As a result, recently, a number of low atmospheric visibility oriented research areas have begun to receive great attention, such as defogging/dehazing [4]–[11], foggy scene understanding [12], [13], visibility estimation [14], etc. Actually, there are a plethora of previous studies focusing on vision problems related to mist or fog. By contrast, natural haze, smog, and dust are rarely investigated, which are also common natural phenomena. Studies on a broader range of atmospheric degradation phenomena can benefit the restoration of images suffering from atmospheric visibility impairment. They are of great significance to vision-based intelligent systems, such as traffic monitoring systems or driving assistance systems.

In most cases, to train and to evaluate vision algorithms that can adapt to low atmospheric visibility conditions, a dataset that comprises a large number of pairs of clear images and their visibility-degraded versions is eagerly desired. However, to collect large amounts of such image pairs from real world is nearly impossible. A feasible solution to conquer this problem is to use virtual simulation technologies, which is also the focus of this paper.

In this work, we focus on how to simulate atmospheric visibility impairment phenomena aroused by changes in aerosol composition and its proportions. Specifically, simulating strategies for five most commonly encountered natural phenomena, mist, fog, natural haze, smog, and Asian dust, are given. In Fig. 1, real world images and our simulation results are shown for comparison. Images in the left column of Fig. 1 are collected from the real world while the ones in the right column are our simulation results. From the first row to the fifth row, the related natural phenomena are mist, fog, natural haze, smog, and Asian dust, respectively. By comparing with the real world images, it can be seen that our simulation results are quite realistic.

The remainder of this paper is organized as follows. Sect. II introduces the related work and our contributions. Sect. III reviews the Koschmieder's law and the Duntley's law in atmosphere science. Our proposed schemes for atmospheric visibility impairment simulation are presented in Sect. IV. Experimental results are reported in Sect. V. Finally, Sect. VI concludes the paper.

II. Related Work and Our Contributions

A. Synthetic Data for Computer Vision

Recent progress in computer vision has been propelled by high capacity models trained on large datasets. Unfortunately, establishing large-scale datasets comprising real images with manual annotations is extremely costly and cumbersome and in some cases is even not feasible. This has spurred the

Manuscript received December 2, 2020; revised June 17, 2021; accepted October 7, 2021. Date of publication October 19, 2021; date of current version October 25, 2021. This work was supported in part by the National Key Research and Development Project under Grant 2020YFB2103900, in part by the National Natural Science Foundation of China under Grant 61973235 and Grant 61936014, in part by the Shanghai Municipal Science and Technology Major Project under Grant 2021SHZDZX0100, and in part by the Fundamental Research Funds for the Central Universities. The associate editor coordinating the review of this manuscript and approving it for publication was Dr. Sen-Ching Samson Cheung. *(Corresponding author: Lin Zhang.)*

Lin Zhang, Anqi Zhu, and Shiyu Zhao are with the School of Software Engineering, Tongji University, Shanghai 201804, China (e-mail: cslinzhang@tongji.edu.cn; 1931555@tongji.edu.cn; shiyuzhao94@gmail.com).

Yicong Zhou is with the Department of Computer and Information Science, University of Macau, Macau, China (e-mail: yicongzhou@um.edu.mo).

Digital Object Identifier 10.1109/TIP.2021.3120044

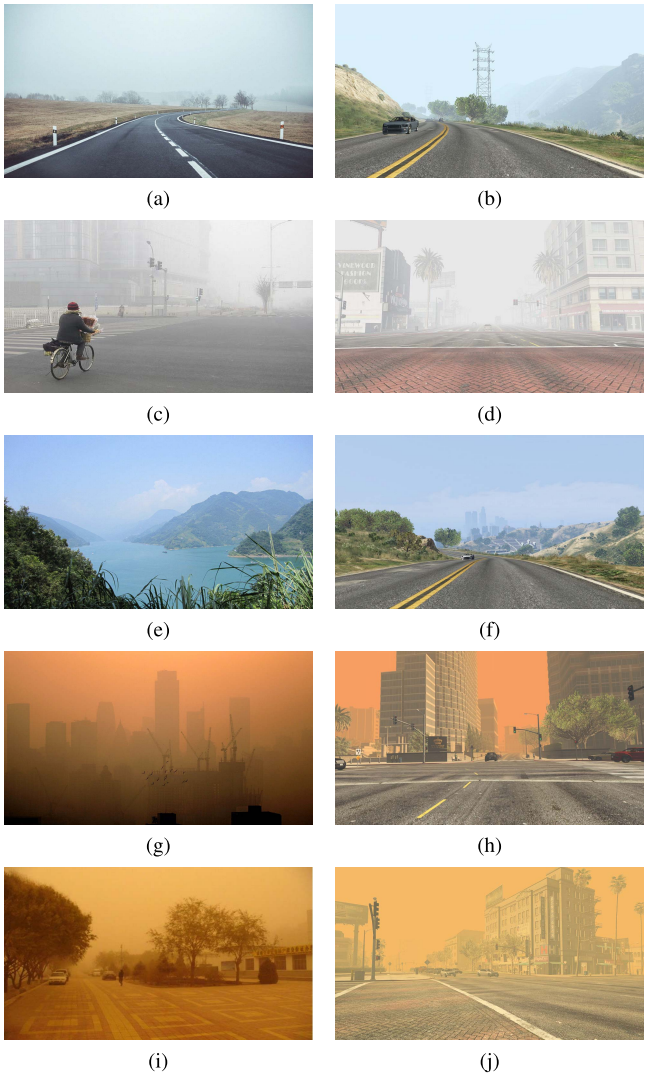

Fig. 1. Real world images and our simulation results are shown for comparison. Images in the left column are collected from the real world while the ones in the right column are simulation results by our proposed schemes. From the first row to the fifth row, the related natural phenomena are mist, fog, natural haze, smog, and Asian dust, respectively.

development of methods for producing photo-realistic, computer generated images with corresponding pixel-level annotations and labels. Generally speaking, using simulation techniques to create training data has the following merits: 1) creating virtual synthetic data is cheaper and easier than collecting real world data; 2) nearly all the relevant factors for rendering images can be controlled, such as objects in the scene, the illumination, the camera pose, etc.; and 3) consistent and accurate annotations usually can be naturally generated as byproducts. More importantly, some studies have confirmed that for some specific applications (e.g. vehicle detection) models trained on synthetic data can generalize quite well to real data [15]. Representative studies focusing on synthetic data generation for solving vision tasks are briefly reviewed as follows.

The first category of schemes in this field rely on simulators created by game engines, such as Unity[1] or Unreal.[2] In [16], Ros *et al*. presented the SYNTHIA dataset, which contains 13,400 annotated frames for the semantic segmentation task. Since the dataset was constructed from a virtual city implemented with Unity, more data could be collected at any time with zero additional budget for annotation. Virtual KITTI [17] is another dataset captured from a virtual city created by Unity. It contains 35 synthetic videos for a total of approximately 17,000 frames, all with automatic ground truth for object detection, tracking, depth, optical flow, as well as scene and instance segmentation at the pixel level. In [18], Müller *et al*. constructed a training and evaluation simulator, namely Sim4CV, which was built on top of Unreal Engine. Sim4CV integrates full featured physics based cars, unmanned aerial vehicles, and animated human actors in diverse urban and suburban 3D environments. Similar as Sim4CV [18], Dosovitskiy *et al*. constructed an open-source simulator for autonomous driving research, namely CARLA (CAR Learning to Act) [19]. CARLA was developed from the ground up to support development, training, and validation of autonomous urban driving systems. As pointed by [20], [21], a shared drawback of these approaches is the significant gap in quality of synthetic images with respect to real world images.

Another category of approaches resort to commercial video games, such as Grand Theft Auto V (GTAV),[3] to produce datasets of photo-realistic scenes and corresponding annotations. It is generally accepted that scenes created in this way are more realistic than those created by simulators directly relying on game engines [20], [21]. In [22], Richter *et al*. proposed the idea of "playing for data" (PFD). PFD relied on inserting middleware between the game engine and the graphics hardware to extract desired information from GTAV without having access to the game's code or content. Later in [20], Richter *et al*. extended their earlier work [22] to generate 25K video frames with ground-truth data for optical flow, semantic instance segmentation, object detection/tracking, object-level 3D scene layout, and visual odometry. In [21], Augus *et al*. established the dataset URSA (Unlimited Road-scene Synthetic Annotation), whose scenes were also extracted from GTAV. Angus *et al*. overcame the inaccessibility of in-game content by leveraging tools traditionally used for game modifications. In [15], Johnson-Roberson *et al*. presented a fully automated system to extract data used to train instance segmentation algorithms from GTAV. Specifically, they extracted data from the game using two plugins, Script Hook V[4] and Script Hook V. Net,[5] developed by the open source community.

B. Existing Studies for Atmospheric Visibility Impairment Simulation

Though preeminent synthetic datasets as reviewed in Sect. II-A have been created to help train vision algorithms, none of them has systematically taken the negative effects of atmospheric visibility impairment into account. Studies focusing on simulation of atmospheric visibility impairment

[1]https://unity3d.com/
[2]https://www.unrealengine.com/
[3]https://www.rockstargames.com/V/
[4]http://www.dev-c.com/gtav/scripthookv/
[5]https://www.gta5-mods.com/tools/scripthookv-net

actually are quite sporadic. In this sub-section, they will be reviewed and analyzed deeply.

To our knowledge, in the field of computer vision, the studies of atmospheric visibility impairment simulation are all about "fog". In addition, all these simulation schemes actually resort to the same physical model, i.g. Koschmieder's law (Eq. 1) for horizontal vision and non-absorbing atmosphere [30].

An earlier work in this field was conducted by Tarel *et al.* [12]. Using the SiVIC^{TM} software which allows to build physically-based road environments, they constructed the dataset FRIDA (Foggy Road Image DAtabase). FRIDA comprises 90 synthetic images of 18 urban road scenes. In their later work [23], Tarel *et al*. upgraded FRIDA to FRIDA2, which contains 330 synthetic images of 66 diverse scenes. Obviously, FRIDA and FRIDA2 are both quite small in scale and actually their images are not realistic-looking.

A quite recent work focusing on synthesizing foggy images is [13]. In [13], Sakaridis *et al*. attempted to address the problem of semantic foggy scene understanding and proposed a pipeline to add synthetic fog to real, clear-weather images in Cityscapes [31]. Sakaridis *et al*.' work has the following potential shortcomings. First, the contrast of images in Cityscapes is not very high since sensors used to collect them were mounted behind the windshield. Thus, it is not appropriate to use Cityscapes images as supervisory signals for some applications, e.g. defogging. Second, the depth information (which is indispensable for fog simulation) in Cityscapes is not complete and its completion is a great challenge itself. An inaccurate depth map will definitely give rise to errors in fog synthesis. Third, the way Sakaridis *et al*. estimated the horizon sky luminance A (see Eq. 1) was questionable. Given an image from Cityscapes, they took the median of all the 0.1% pixels with largest dark channel values as A. Actually, such a method to estimate A makes sense only when the sky is overcast. According to Koschmieder's law [30], strictly speaking, A should be the luminance of the horizon sky. When the weather is overcast, we can assume that the sky luminance is uniform across all the sky regions. However, such an assumption does not hold for most Cityscapes images since they were collected on clear days.

In [6], Li *et al*. established a dataset RESIDE (REalistic Single-Image DEhazing) and performed a thorough evaluation of single-image defogging algorithms. RESIDE comprises both indoor and outdoor scenes and we refer to them as "RESIDE-indoor" and "RESIDE-outdoor", respectively. For indoor foggy scene synthesis, they made use of images with depth maps selected from NYU2 [32] and Middlebury stereo [33]. For the outdoor case, they collected 2,071 real world outdoor images and resorted to [34] to estimate the depth map from each image. The simulation pipeline of RESIDE-indoor actually violates the premise that Koschmieder's law is established. In Koschmieder's law (Eq. 1), A should be the luminance of the horizon sky; however, for indoor scenes, no sky exists. Furthermore, Koschmieder's law assumes that the linear dimensions of the objects in the scene are small in comparison to their distances from the observer, which does not hold either for indoor scenes. The potential risk of RESIDE-outdoor lies in its way to generate depth maps. Depth maps estimated by a computational model are usually not reliable since singe-image based depth estimation is a highly ill-posed, still open problem. Unreliable depth maps can make the simulation results unpredictable and less useful.[6]

In the field of image defogging, to train and validate defogging models, researchers usually used depth datasets comprising clear images and associated depth maps to create synthetic foggy scenes. Most of them [5], [8], [9], [24], [25] resorted to indoor depth datasets (such as NYU2 [32], Middlebury stereo [33], and SUN3D [35]) and of course the synthesized results suffer from the same problem as "RESIDE-indoor". Another few of them, e.g. Li *et al*.'s work [7], used the outdoor depth dataset Make3D [36]. However, the depth information in Make3D is not precise. As pointed in [6], Make3D has at least 4 meters of average error.

It can be regarded as a physical way to simulate foggy image by using fog/haze machines to generate a dense vapor [26]–[29]. Actually, the images in these datasets [26]–[29] were taken from quite few viewpoints, limiting their scene varieties. I-HAZE [26] only contains 35 indoor scenes, O-HAZE [27] contains 45 outdoor scenes, Dense-Haze [28] contains 33 outdoor scenes and 22 indoor scenes, and NH-Haze [29] contains 55 outdoor scenes. The small scales of these datasets make them only suitable for performance evaluation of defogging algorithms, not for large-scale model training. When collecting the datasets [26]–[29], the researchers first recorded the ground truth (haze-free image) and then immediately started introducing fog in the scene. However, the produced fog covers a much smaller area than the area covered by natural fog. Additionally, since the haze-free image and its foggy version are not shot at the same time, these schemes cannot avoid small changes in the same scene, such as leaves, lawns, etc. What's more, the collection cost of these methods of using fog/haze machines is very high.

Shortcomings or irrationalities of existing studies focusing on foggy scene synthesis are summarized in Table I.

C. Our Motivations and Contributions

Having investigated the literature, we find that existing studies of atmospheric visibility impairment simulation have limitations in at least three aspects.

First, the vast majority of researchers in the field of CV actually do not notice the difference between "fog" and "haze". These two words are often mixed incorrectly.

Second, as reviewed in Sect. II-B, many researchers are not aware that their foggy scene simulation schemes actually are not quite reasonable. For synthesizing fog, all the schemes used Koschmieder's law [30]. However, the conditions under which Koschmieder's law could hold are often mistakenly ignored.

Third, the existing studies of atmospheric visibility impairment simulation are all about "fog". Other commonly encountered natural phenomena that can also cause visibility

[6] An example can be found in Fig. 6.

TABLE I
SHORTCOMINGS OR IRRATIONALITIES OF EXISTING STUDIES OF FOGGY SCENE SYNTHESIS

dataset name	indoor or outdoor?	shortcomings or irrationalities
FRIDA [12] and FRIDA2 [23]	outdoor	1. The scale of the dataset is quite small. 2. The synthesized results are not photo-realistic.
Foggy Cityscapes [13]	outdoor	1. The contrast of the clear images is not high. 2. The depth information output by the depth completion model may not be reliable. 3. The way to set the horizon sky luminance A is not reasonable.
RESIDE-indoor [6]	indoor	It violates the premise that Koschmieder's law is established.
RESIDE-outdoor [6]	outdoor	Depth maps are not reliable since they are estimated using a "depth from a single-image" model.
Ren *et al.*'s dataset [9]	indoor	It violates the premise that Koschmieder's law is established.
Li *et al.*'s dataset [5]	indoor	It violates the premise that Koschmieder's law is established.
D-Hazy [24]	indoor	It violates the premise that Koschmieder's law is established.
Li *et al.*'s dataset [7]	indoor and outdoor	1. Indoor foggy scene simulation violates the premise that the Koschmieder's law is established. 2. Outdoor foggy scene simulation suffers from the poor quality of the depth maps in Make3D.
Zhang *et al.*'s dataset [25]	indoor	It violates the premise that Koschmieder's law is established.
I-HAZE [26] O-HAZE [27] Dense-Haze [28] NH-Haze [29]	indoor outdoor indoor and outdoor outdoor	1. The scale of the dataset is quite small. 2. The produced fog covers a much smaller area than the area covered by natural fog. 3. There are inevitable differences between the scenes of the haze-free image and its corresponding hazy version. 4. The collection cost of using fog/haze machines is very high.

degradation (such as mist, smog, Asian dust, etc.) have not been considered.

In this work, we attempt to fill the aforementioned research gaps to some extent and our major contributions are summarized as follows.

(1) We clearly point out that fog and haze have different physical origins and optical properties. Hence, these two words cannot be used interchangeably. From the view of optics, the inherent difference between fog and haze is that their extinction coefficients have different optical properties. Firstly, the extinction coefficient of fog is wavelength independent which is not true for haze. Secondly, in foggy days, the light absorption can be neglected; however, for most cases of haze, the light absorption should be taken into account. In other words, fog and haze should be described by different physical models.

(2) Conditions under which Koschmieder's law can hold are stated explicitly. For a long time, these conditions have not caught the attention of CV researchers. In addition, we point out that if the light absorption needs to be considered, Duntley's law (Eq. 4) [37] is a valid model candidate instead of Koschmieder's law. To our knowledge, we are the first to introduce Duntley's law to the CV field.

(3) We present simulation schemes for five commonly encountered atmospheric visibility impairment phenomena. Based on a thorough investigation of the relevant studies in atmospheric science, we set up computational models for mist, fog (both homogenous and heterogeneous), natural haze, smog, and Asian dust. To our knowledge, our work is the first in the CV field to give schemes for simulating atmospheric visibility impairment phenomena other than fog. As a byproduct, with the proposed simulation strategies, we have constructed an Atmospheric Visibility Impairment Dataset, AVID for short. To obtain clear images and the associated depth maps, we resort to GTAV since quite a number of previous studies have corroborated that scenes created by GTAV are quite photo-realistic. AVID comprises 40,000 clear source images (with associated depth maps). For each clear image, 20 visibility-impaired versions are created, and thus AVID contains 800,000 visibility-impaired images. AVID can be explored to train algorithms for restoring images with atmospheric visibility impairment or algorithms of image-based visibility estimation.

III. KOSCHMIEDER'S LAW AND DUNTLEY'S LAW

In atmospheric science, Koschmieder's law [30] is widely used to model the relationship among factors of the apparent luminance, the intrinsic luminance, the extinction coefficient, and the observing distance. It can be expressed as,

$$L(\lambda) = L_0(\lambda)\, e^{-b(\lambda)d} + A(\lambda)\left(1 - e^{-b(\lambda)d}\right) \tag{1}$$

where $L(\lambda)$ is the observed luminance, $L_0(\lambda)$ is the clear scene radiance, $A(\lambda)$ is the luminance of the horizon sky, $b(\lambda)$ is the extinction coefficient of the atmosphere, and λ is the light wavelength. The extinction coefficient $b(\lambda)$ can be depicted as the sum of several components [38],

$$b(\lambda) = b_{Rayleigh}(\lambda) + b_{scat}(\lambda) + b_{abs-gas}(\lambda) + b_{abs-aero}(\lambda) \tag{2}$$

where $b_{Rayleigh}(\lambda)$ represents the scattering due to gaseous air (the blue-sky scatter), $b_{scat}(\lambda)$ represents the component due to light scattering by aerosol, and $b_{abs-gas}(\lambda)$ and $b_{abs-aero}(\lambda)$ represent the absorption due to gases and particles, respectively. In the literature, a convenient and easily visualized substitute for the extinction coefficient is the "visibility" (also called "meteorological range"). The visibility v has the following relationship with the extinction coefficient $b(\lambda)$ [30], [38],

$$v = -\frac{\ln 0.05}{b(\lambda)_{|\lambda=550nm}} \tag{3}$$

Actually, all the existing schemes for synthesizing foggy scenes are based on Koschmieder's law (Eq. 1). However, few of them has noticed that there are several assumptions to make it hold [30]. These assumptions are listed as follows.

(a) Koschmider's law applies only to horizontal vision; otherwise, the extinction coefficient $b(\lambda)$ cannot be considered as a constant along the sight path.

(b) It applies only to non-absorbing atmosphere. In other words, if the atmospheric absorption should be taken into account, this law cannot be used.

(c) It assumes that the surface of the earth is considered as a uniform horizontal plane, implying that all parts of the atmosphere in the horizontal plane are equally illuminated.

(d) The extinction coefficient (with respect to a specific light wavelength) is constant in the horizontal plane along the sight path.

(e) The linear dimensions of the object are small in comparison to its distance from the observer.

The main difference between Koschmieder's law and Duntley's law is whether the atmospheric absorption is considered. If the atmospheric absorption should be considered, we must adopt a slightly different physical model developed by Duntley [37]. Duntley's law can be expressed as,

$$L(\lambda) = L_0(\lambda)\, e^{-b(\lambda)d} + \frac{L_a(\lambda)}{b(\lambda)}\left(1 - e^{-b(\lambda)d}\right) \tag{4}$$

where $L_a(\lambda)$ is the constant luminance of the air between the object and the observer. Except that the atmosphere can be absorbing, all the other conditions to make Koschmieder's law hold are also required by Duntley's law.

Koschmieder's law and Duntley's law will be explored by us for atmospheric visibility impairment simulation. Sect. IV gives details.

IV. Schemes for Atmospheric Visibility Impairment Simulation

In this section, schemes for simulating five most commonly encountered atmospheric visibility impairment phenomena, including mist, fog, natural haze, smog, and Asian dust, are presented. At first, it needs to be emphasized that when atmospheric visibility impairment happens, the associated $b_{Rayleigh}(\lambda)$ is much smaller than $b_{scat}(\lambda) + b_{abs-gas}(\lambda) + b_{abs-aero}(\lambda)$ and can be omitted when modeling. Thus, in the following parts of this section, $b(\lambda)$ is simplified from Eq. 2 to Eq. 5,

$$b(\lambda) = b_{scat}(\lambda) + b_{abs-gas}(\lambda) + b_{abs-aero}(\lambda) \tag{5}$$

Details of proposed simulation pipelines for mist, fog, natural haze, smog, and Asian dust are presented in Sect. IV-A, Sec. IV-B, Sect. IV-C, Sect. IV-D, and Sect. IV-E, respectively. How to determine the horizon sky luminance A and how to get the clear scene $L_0(\lambda)$ and the associate depth map are introduced in Sect. IV-F.

A. Mist

Condensation of water vapour on atmospheric nuclei leads to the formation of mist and fog [39]. The only difference between mist and fog lies in the visibility. The term "fog" refers to a state of the atmosphere for which the visibility is less than $1,000m$ while for "mist", the "visibility" is greater than $1,000m$ [39].

Compared to the scattering, the effect of light absorption is negligible in the water droplets. In his masterpiece [30], Middleton pointed out that even serious pollution of the cloud droplets has little effect on the spectral radiance of the overcast sky. Thus, for modeling mist or fog, $b_{abs-gas}(\lambda)$ and $b_{abs-aero}(\lambda)$ can be omitted and we only need to consider one term $b_{scat}(\lambda)$.

For mist or fog, water droplets are larger compared with the wavelength in the visible region. Thus, the effect of scattering may then be deduced by geometrical optics and is independent of wavelength [30], [39]. Consequently, $b_{scat}(\lambda)$ does not depend on λ anymore and we denote it by b^{Δ}_{scat}.

For mist/fog, since the light absorption can be neglected, we use Koschmieder's law (Eq. 1) for its simulation. In implementation, the synthesized scene has RGB three channels. Concrete formulas to generate them are given below,

$$\begin{cases} L^R(\mathbf{x}) = L_0^R(\mathbf{x})\, e^{-b^{\Delta}_{scat} d(\mathbf{x})} + A^R\left(1 - e^{-b^{\Delta}_{scat} d(\mathbf{x})}\right) \\ L^G(\mathbf{x}) = L_0^G(\mathbf{x})\, e^{-b^{\Delta}_{scat} d(\mathbf{x})} + A^G\left(1 - e^{-b^{\Delta}_{scat} d(\mathbf{x})}\right) \\ L^B(\mathbf{x}) = L_0^B(\mathbf{x})\, e^{-b^{\Delta}_{scat} d(\mathbf{x})} + A^B\left(1 - e^{-b^{\Delta}_{scat} d(\mathbf{x})}\right) \end{cases} \tag{6}$$

where $\left(L^R(\mathbf{x}), L^G(\mathbf{x}), L^B(\mathbf{x})\right)$ are the RGB values of the synthesized image at the position $\mathbf{x}$, $\left(L_0^R(\mathbf{x}), L_0^G(\mathbf{x}), L_0^B(\mathbf{x})\right)$ are the RGB values of the clear scene at $\mathbf{x}$, $d(\mathbf{x})$ is the scene depth at $\mathbf{x}$, and $\left(A^R, A^G, A^B\right)$ specifies the horizon sky luminance.

For constructing AVID, from each clear image, three mist scenes were synthesized, whose visibilities were randomly chosen from the ranges $[1000m, 3000m)$, $[3000m, 5000m)$, and $[5000m, 10000m)$, respectively. Given the visibility, b^{Δ}_{scat} can be computed by Eq. 3.

B. Fog

As we have mentioned, fog can be actually seen as "dense mist" and can also be modeled by Eq. 6. According to National Standard of China [40], fog can be classified as four levels based on its visibility, heavy fog, thick fog, dense fog, and super-dense fog, whose visibility ranges are $[500m, 1000m)$, $[200m, 500m)$, $[50m, 200m)$, and $[0m, 50m)$. As a result, when constructing AVID, from each clear image, four foggy scenes were synthesized, whose visibilities were randomly chosen from the ranges $[500m, 1000m)$, $[200m, 500m)$, $[50m, 200m)$, and $[15m, 50m)$, respectively.

It can be noticed that with the aforementioned fog simulation strategy, the whole foggy scene has the same extinction coefficient. That means the whole scene has the same fog density everywhere. Such fog is called "homogenous fog". However, the natural phenomena usually do not change in regular ways but have a large degree of randomness. Such a feature is also present in fog. Sometimes, fog will have irregular shapes due to wind and air turbulence, which is referred to as "heterogeneous fog". Perlin noise [41] has been proved to be a good choice to simulate random visual effects in nature. Thus, to simulate heterogenous fog, we multiply a random perturbation specified by Perlin noise [41] to the scene's extinction coefficients and thus the extinction coefficient at $\mathbf{x}$ denoted by $b^{\Delta}_{scat}(\mathbf{x})$ can be expressed as $b^{\Delta}_{scat}(\mathbf{x}) = b^{\Delta}_{scat} \cdot perlin\_noise(\mathbf{x})$. When constructing AVID, from each clear image, two heterogenous foggy images were created for "thick fog" and "dense fog".

C. Natural Haze

Haze often occurs when dust and smoke particles accumulate in relatively dry air. In hazy days, extremely small, dry particles suspend in the air and give the air an opalescent appearance. It needs to be stressed that different from fog the extinction coefficient of haze is wavelength dependant [39]. According to the degree related to industrial pollution, haze can be further classified as "natural haze" and "smog" (refer to Sect. IV-D) [42]. Natural haze is mild and is not related to industrial pollution. A typical example of the natural haze is the "blue haze" phenomenon, in which nano-particles are formed by the interaction between biogenic organic acids and sulfuric acid [43]. Blue haze often happens over forested areas.

Since natural haze contains little pollutants, its absorption effect on solar radiation can be neglected and thus $b_{abs-gas}(\lambda)$ and $b_{abs-aero}(\lambda)$ can be omitted. As a result, when simulating natural haze, with respect to its extinction coefficient, we only need to consider the part $b_{scat}(\lambda)$ and for the sake of clarity we denote it by $b_{scat}^{NH}(\lambda)$ in the context of natural haze.

In atmospheric science, scientists suggest that $b_{scat}^{NH}(\lambda)$ can be well modeled as [30], [39],

$$b_{scat}^{NH}(\lambda) = C \cdot \lambda^{-\gamma} \tag{7}$$

where C and γ are two constants. C is determined by the visibility. For determining γ, some empirical studies have been conducted and suggest that [39],

$$\gamma = \begin{cases} 1.3, & if\ 6km < v < 20km \\ 0.585 v^{1/3}, & if\ 0km < v \leq 6km \end{cases} \tag{8}$$

where v represents the visibility. If v and γ are given, C can be derived from Eq. 3 and Eq. 7 and expressed as,

$$C = \frac{-\ln 0.05}{(550)^{-\gamma} v} \tag{9}$$

For natural haze, as the light absorption can be ignored, we use Koschmieder's law (Eq. 1) for its simulation. Since $b_{scat}^{NH}(\lambda)$ is dependant on wavelength λ, to synthesize scenes represented by RGB images, we must know the wavelengths for the three primary colors. According to CIE1964, the wavelengths for the three primary colors, red, green, and blue are $645.2nm$, $526.3nm$, and $444.4nm$, respectively [44]. Concrete formulas to synthesize RGB images with natural haze are then given as,

$$\begin{cases} L^R(\mathbf{x}) = L_0^R(\mathbf{x}) e^{\frac{-C \cdot d(\mathbf{x})}{(645.2)^\alpha}} + A^R \left(1 - e^{\frac{-C \cdot d(\mathbf{x})}{(645.2)^\alpha}}\right) \\ L^G(\mathbf{x}) = L_0^G(\mathbf{x}) e^{\frac{-C \cdot d(\mathbf{x})}{(526.3)^\alpha}} + A^G \left(1 - e^{\frac{-C \cdot d(\mathbf{x})}{(526.3)^\alpha}}\right) \\ L^B(\mathbf{x}) = L_0^B(\mathbf{x}) e^{\frac{-C \cdot d(\mathbf{x})}{(444.4)^\alpha}} + A^B \left(1 - e^{\frac{-C \cdot d(\mathbf{x})}{(444.4)^\alpha}}\right) \end{cases} \tag{10}$$

When establishing AVID, from each clear image, four images with natural haze were synthesized, whose visibilities were randomly chosen from the ranges $[1km, 2km)$, $[2km, 4km)$, $[4km, 6km)$, and $[6km, 20km)$, respectively.

D. Smog

When the haze is heavy and is highly relevant to industrial pollution, it is referred to as "smog". The word smog was coined in the early 20th century as a portmanteau of the words smoke and fog [45]. This kind of visible air pollution is composed of nitrogen oxides, sulphur oxides, ozone, smoke or dirt particles and also less visible particles. Human-made smog is derived from coal emissions, vehicular emissions, industrial emissions, forest and agricultural fires and photochemical reactions of these emissions.

Typically, smog has a reddish-brown or yellowish-brown color [46], mainly owing to the light absorption at shorter wavelengths by the gases (e.g. NO_2 [38], [47]) and particles (e.g. black carbon [48], [49], organic carbon [48], and mineral dust [49], [50]) in the smog. Therefore, for modeling smog, all the three terms $b_{scat}(\lambda)$, $b_{abs-gas}(\lambda)$, and $b_{abs-aero}(\lambda)$ of the extinction coefficient $b(\lambda)$ should be considered.

For smog, $b_{scat}(\lambda)$ was found empirically to be an inverse power function of wavelength in the visible band and can be expressed as [51],

$$b_{scat}(\lambda) = C_1 \cdot \lambda^{-\alpha}, \quad \alpha \in [1.3, 2.3] \tag{11}$$

where C_1 is a constant related to the visibility. The main source of gas for light absorption at the visible band is NO_2 and according to [52], $b_{abs-gas}(\lambda)$ (when the gas is NO_2) roughly conforms to the following relations,

$$b_{abs-gas}(\lambda) = \begin{cases} C_2 \cdot \lambda^{-3}, & for\ blue\ light \\ C_2 \cdot \lambda^{-4}, & for\ green\ or\ red\ light \end{cases} \tag{12}$$

For smog, $b_{abs-aero}(\lambda)$ has also been studied and can be parameterized using a power law relationship [48],

$$b_{abs-aero}(\lambda) = C_3 \cdot \lambda^{-\beta}, \quad \beta \in [1, 2] \tag{13}$$

Since light absorption should be taken into account, Duntley's law (Eq. 4) is used for smog simulation. As a result, formulas to synthesize RGB scenes with smog are,

$$\begin{cases} L^R(\mathbf{x}) = L_0^R(\mathbf{x}) e^{-b^R d(\mathbf{x})} + \frac{L_a^R}{b^R}\left(1 - e^{-b^R d(\mathbf{x})}\right) \\ L^G(\mathbf{x}) = L_0^G(\mathbf{x}) e^{-b^G d(\mathbf{x})} + \frac{L_a^G}{b^G}\left(1 - e^{-b^G d(\mathbf{x})}\right) \\ L^B(\mathbf{x}) = L_0^B(\mathbf{x}) e^{-b^B d(\mathbf{x})} + \frac{L_a^B}{b^B}\left(1 - e^{-b^B d(\mathbf{x})}\right) \end{cases} \tag{14}$$

For implementation, we need to determine $\left(L_a^R, L_a^G, L_a^B\right)$ and $\left(b^R, b^G, b^B\right)$. By some mathematical derivations and approximations, we can get the following equations,

$$\begin{cases} L_a^R = k^R b^R A^R \\ L_a^G = k^R k^{RG} b^R A^G \\ L_a^B = k^R k^{RB} b^R A^B \\ b^G = \dfrac{-\ln 0.05}{v} \\ b^R = C^{RG} b^G \\ b^B = \dfrac{b^R}{C^{RB}} \end{cases} \tag{15}$$

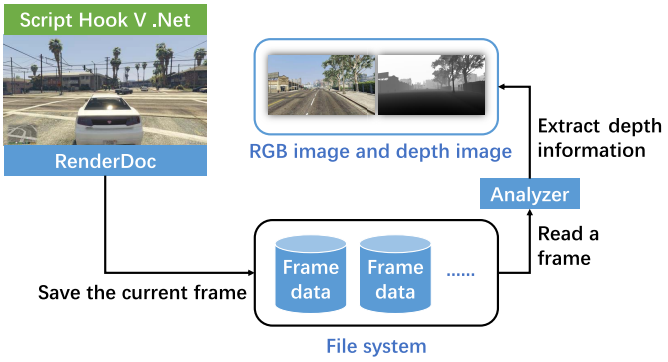

Fig. 2. The pipeline for acquiring images and corresponding depth maps from GTAV.

where $k^R \in (0.9, 1)$, $k^{RG} \in \left(\frac{0.8}{k^R}, \frac{1.2}{k^R}\right)$, $k^{RB} \in \left(\frac{0.8}{k^R}, \frac{1.2}{k^R}\right)$, v is the visibility, $C^{RG} \in \left[\frac{645.2^{-4}}{526.3^{-4}}, \frac{645.2^{-1}}{526.3^{-1}}\right]$, and $C^{RB} \in \left[\frac{645.2^{-4}}{444.4^{-3}}, \frac{645.2^{-1}}{444.4^{-1}}\right] \cap \left[C^{RG}\frac{526.3^{-4}}{444.4^{-3}}, C^{RG}\frac{526.3^{-1}}{444.4^{-1}}\right]$. With respect to detailed derivations for Eq. 15, please refer to Appendix A. When simulating smog, k^R, k^{RG}, k^{RB}, C^{RG}, and C^{RB} are randomly selected from their possible value ranges.

When constructing AVID, from each clear image, three versions with smog were synthesized, whose visibilities were randomly chosen from the ranges $[50m, 100m)$, $[200m, 500m)$, and $[500m, 1000m)$, respectively.

E. Asian Dust

Asian dust, also called "yellow dust", "yellow sand", or "China dust storms", is a meteorological phenomenon which affects much of East Asia year round but especially during the spring months [53]. The dust originates in the deserts of Mongolia, northern China and Kazakhstan where high-speed surface winds and intense dust storms kick up dense clouds of fine, dry soil particles. These clouds are then carried eastward by prevailing winds and pass over China, North and South Korea, and Japan, as well as parts of the Russian Far East.

The solid particles of Asian dust mainly come from crustal sources. The mass concentration of mineral ions, such as Mg^{2+}, K^+, Na^+, and Ca^{2+}, which came mainly from natural dust sources, is higher during Asian dust days compared to normal or smog days [54]. Stronger absorption at shorter wavelengths could arise due to the presence of mineral dusts in atmospheric aerosols [49]. In Asian dust days, the concentration of nitrogen oxides is similar as normal days [54]. Thus, when modeling Asian dust, $b_{abs-gas}(\lambda)$ can be neglected and only two terms $b_{scat}(\lambda)$ and $b_{abs-aero}(\lambda)$ need to be considered. That is, for Asian dust days, the extinction coefficient is $b(\lambda) = b_{scat}(\lambda) + b_{abs-aero}(\lambda)$.

For Asian dust, $b_{scat}(\lambda)$ can be modeled as the form Eq. 11 and $b_{abs-aero}(\lambda)$ can be modeled as the form Eq. 13. Since light absorption should be taken into account in Asian dust days, we also need to resort to Duntley's law for its simulation. Consequently, Asian dust can also be simulated by Eq. 14 and Eq. 15. Actually, it can be noticed that the strategy for simulating Asian dust is quite similar to that used for simulating smog. The only exception is that $b_{abs-gas}(\lambda)$ is omitted for the Asian dust case. That will lead to changes of the value ranges of C^{RG} and C^{RB} compared with the smog case. Specifically, for Asian dust simulation, C^{RG} and C^{RB} are specified as $C^{RG} \in \left[\frac{645.2^{-2.3}}{526.3^{-2.3}}, \frac{645.2^{-1}}{526.3^{-1}}\right]$ and $C^{RB} \in \left[\frac{645.2^{-2.3}}{444.4^{-2.3}}, \frac{645.2^{-1}}{444.4^{-1}}\right] \cap \left[C^{RG}\frac{526.3^{-2.3}}{444.4^{-2.3}}, C^{RG}\frac{526.3^{-1}}{444.4^{-1}}\right]$. Details can be found in Appendix B.

When constructing AVID, from each clear image, 4 versions with Asian dust were synthesized, whose visibilities were randomly chosen form the ranges $[15m, 50m)$, $[50m, 500m)$, $[500m, 1000m)$, and $[1000m, 10000m)$, respectively.

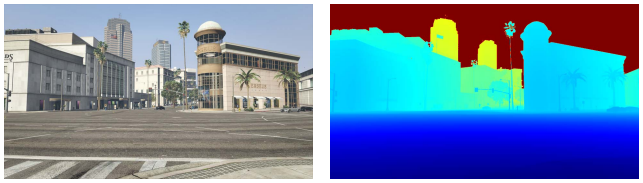

(a) (b)

Fig. 3. (a) is an RGB image extracted from GTAV and (b) is its depth map.

F. Strategies to Get the Horizon Sky Luminance, the Clear Scene, and the Scene Depth

For the aforementioned simulation pipelines, three common issues have not been discussed yet, including how to get the horizon sky luminance $\left(A^R, A^G, A^B\right)$, how to get the clear scene $\left(L_0^R(\mathbf{x}), L_0^G(\mathbf{x}), L_0^B(\mathbf{x})\right)$ and the associated depth map $d(\mathbf{x})$. They are presented in detail in this subsection.

In overcast weather, the sunlight happens Mie scattering in the atmosphere and hence the sky luminance can be considered as nearly uniform. The luminance of any sky region is roughly equal to the luminance of the horizon sky. Based on this prior knowledge, we collected 500 typical real foggy images and recorded their sky luminance vectors as $\left\{skylum_i : |skylum_i \in \mathcal{R}^3\right\}_{i=1}^{500}$. When a $\left(A^R, A^G, A^B\right)$ is desired, it can be randomly selected from $\{skylum_i\}$.

From the conditions that Koschmieder's law or Duntley's law should satisfy, it can be known that the atmospheric visibility impairment simulation can only be conducted on outdoor scenes. However, to get accurate depth information for real-world outdoor scenes is a formidable task. Therefore, in this paper, we resort to GTAV to collect clear outdoor images with corresponding depth maps. GTAV is famous for its photo-realistic rendering and extensive content. The most obvious advantage to using such an open-world video game to collect data is that we can get accurate depth maps programmable. The publisher of GTAV allows non-commercial use of footage from the game. The implementation details are shown in Fig. 2. We follow the detouring strategy proposed in [22] and make use of RenderDoc,[7] a graphics debugging tool, to acquire images and corresponding depth maps from GTAV. Specifically, we took advantage of some game auxiliary

[7] https://renderdoc.org/

Fig. 4. Sample images in our large-scale synthetic image dataset AVID, which comprises 40,000 clear source images (with depth maps) along with their 800,000 visibility-impaired versions.

TABLE II
CHARACTERISTICS OF DATASETS RELATED TO ATMOSPHERIC VISIBILITY IMPAIRMENT SIMULATION

dataset name	conform to Koschmieder's law or Duntley's law?	types of visibility impairment	accurate depth?	real or synthetic src images?	no. src images	no. images with visibility impairment
FRIDA [12]	YES	uniform fog, heterogeneous fog	YES	synthetic	18	72
FRIDA2 [23]	YES	uniform fog, heterogeneous fog	YES	synthetic	66	264
Foggy Cityscapes [13]	YES	uniform fog	NO	real	24,997	34,997
RESIDE-indoor [6]	NO	uniform fog	YES	real	1,899	14,490
RESIDE-outdoor [6]	YES	uniform fog	NO	real	2,071	72,145
Ren *et al.*'s dataset [9]	NO	uniform fog	YES	real	6,000	18,000
Li *et al.*'s dataset [5]	NO	uniform fog	YES	real	1,449	27,256
Zhang *et al.*'s dataset [25]	NO	uniform fog	YES	real	1,050	4,200
D-Hazy [24]	NO	uniform fog	YES	real	1,472	1,472
AVID	YES	mist, uniform fog, heterogeneous fog natural haze, smog, Asian dust	YES	synthetic	40,000	800,000

functions provided by Script Hook V.Net, such as character roaming and automatic driving, to achieve automated data collection. Then the depth is computed as the z-axis value with respect to the standard equipment coordinate system. Frame data collection and information extraction are time-consuming, and thus for the sake of efficiency, we build an asynchronous data acquisition scheme to analyze the data of previous frames while collecting the current frame. In Fig. 3, a sample clear image and its depth map extracted from GTAV are shown.

V. EXPERIMENTAL RESULTS

In experiments, we want to demonstrate that the proposed simulation strategies are feasible and the simulation results are vivid and photo-realistic. In addition, we want to show that the collected dataset AVID is superior to other existing relevant datasets on key indicators. To make our results fully reproducible, the codes and the data have been released at https://cslinzhang.github.io/AVID/.

A. Atmospheric Visibility Impairment Dataset

With the proposed simulation pipelines introduced in Sect. IV, we constructed a large-scale synthetic image dataset, namely Atmospheric Visibility Impairment Dataset, AVID for short. Specifically, we collected 40,000 clear images with associated depth maps from GTAV. For each clear source image, 20 visibility-impaired versions were synthesized, including 3 versions with mist, 4 versions with homogeneous fog, 2 versions with heterogeneous fog, 4 versions with natural haze, 3 versions with smog, and 4 versions with Asian dust. Thus, altogether, AVID comprises 40,000 clear source images (with depth maps) along with their 800,000 visibility-impaired versions. Fig. 4 shows a variety of photo-realistic scenes in AVID.

B. Qualitative Evaluation

In this subsection, we qualitatively compare AVID and the relevant datasets in the literature, including FRIDA [12], FRIDA2 [23], Foggy Cityscapes [13], RESIDE-indoor [6], RESIDE-outdoor [6], Ren *et al.*'s dataset [9], Li *et al.*'s dataset [5], Zhang *et al.*'s dataset [25], and D-Hazy [24]. Their characteristics in terms of "whether conforms to Koschmieder's law or Duntley's law?", "types of visibility impairment", "has accurate depth?", "uses real or synthetic source images?", "number of source images", and "number of images with visibility impairment" are summarized in Table II.

The results in Table II lead us to the following conclusions. First, only a half of the datasets conform to Koschmieder's law or Duntley's law. They are FRIDA [12], FRIDA2 [23], Foggy Cityscapes [13], RESIDE-outdoor [6], and AVID. The simulation pipelines of the other datasets actually are not physically reasonable and the reasons have been analyzed in Sect. II-B. Second, the types of visibility impairment included in AVID are much more versatile. Specifically, the compared datasets only contain foggy scenes while AVID contains four more visibility impairment types, including mist, natural haze, smog,

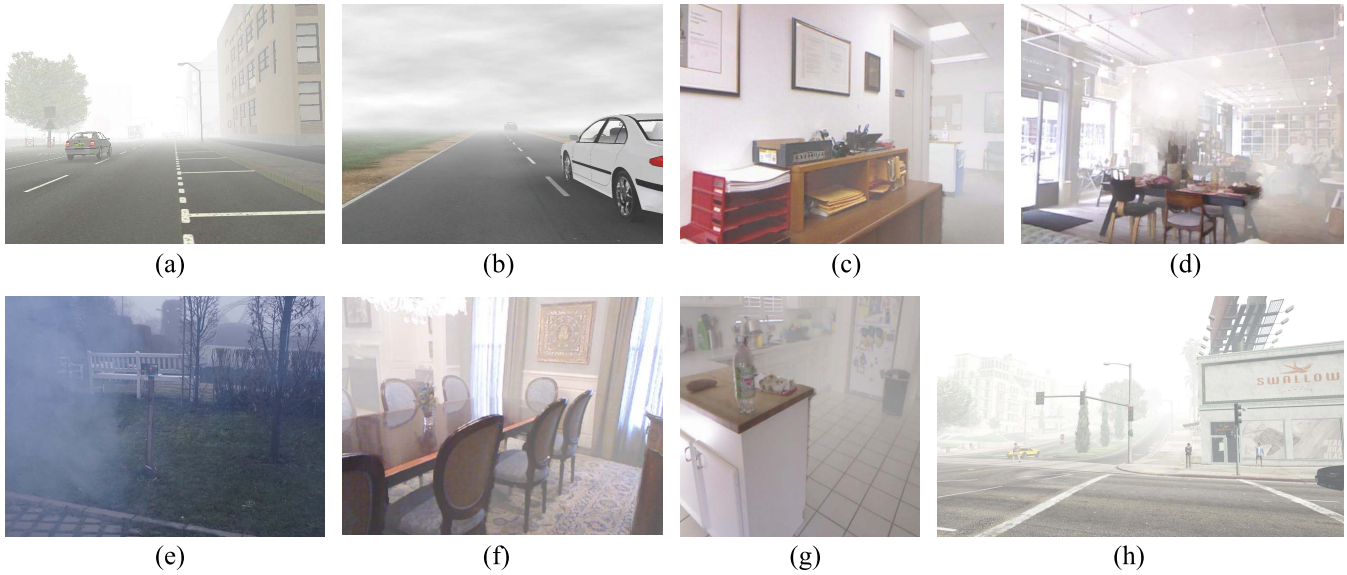

Fig. 5. Samples in datasets related to atmospheric visibility impairment simulation. (a) is selected from FRIDA [12]. (b) is from FRIDA2 [23]. (c) is selected from Li *et al.*'s dataset [5]. (d) is from D-Hazy [24]. (e) is from NH-Haze [29]. (f) is from RESIDE-indoor [6]. (g) is from Zhang *et al.*'s dataset [25]. (h) is from AVID.

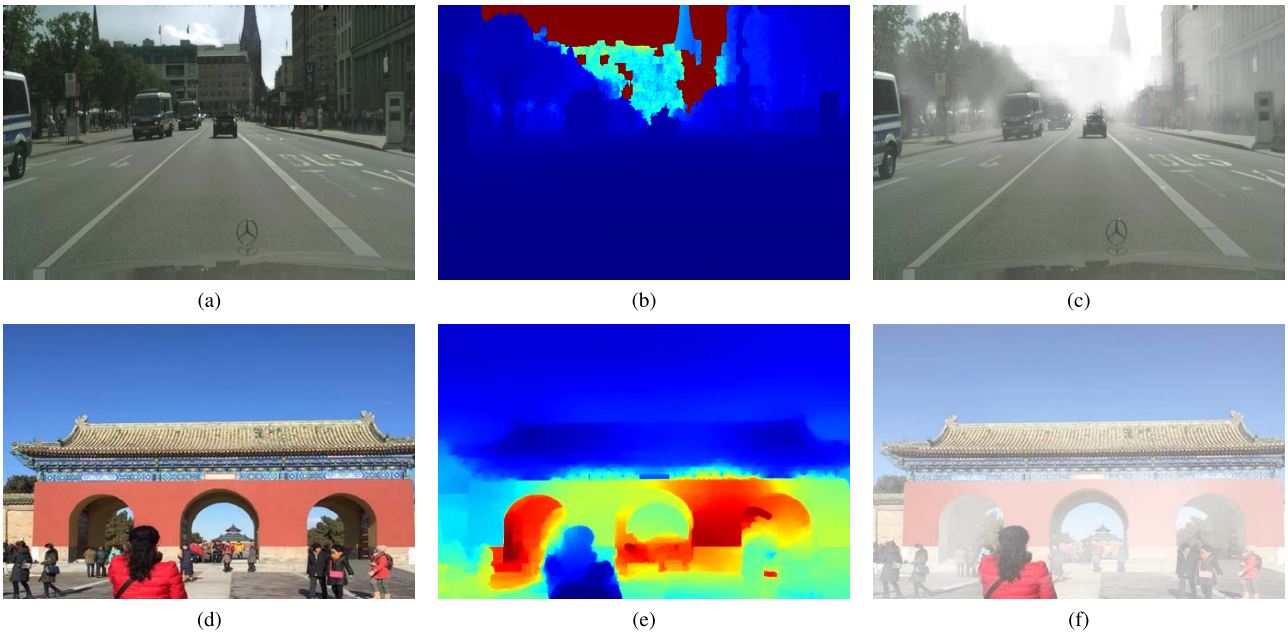

Fig. 6. (a) and (d) are clear images selected from foggy Cityscapes [13] and RESIDE-outdoor [6], respectively. (b) is (a)'s depth map obtained by a depth map completion algorithm [13]. (e) is (d)'s depth map obtained by using a "depth map from a single-image" method [34]. Apparent errors can be observed on (b) and (d), leading to weird simulation results as shown in (c) and (f).

and Asian dust. Third, Foggy Cityscapes [13] and RESIDE-outdoor [6] do not have accurate depth maps, which will surely reduce the quality of the synthesized results. Fourth, AVID is much larger in scale both with respect to the number of clear source images and the number of visibility-impaired ones. In short, AVID is superior to existing relevant datasets on nearly all the key indicators, making it a better candidate to train vision algorithms in which the atmospheric visibility impairment should be considered, e.g. image restoration from visibility-impaired outdoor images or image-based visibility estimation.

C. Realness Evaluation

Realness degree is a key metric to evaluate the quality of a dataset constructed to simulate natural phenomena. Thus, in this experiment, to assess the realness of AVID in comparison with other synthetic datasets, we conducted a perceptual study.

Fig. 5 provides some samples selected from the datasets related to atmospheric visibility impairment simulation. Among the relevant datasets, RESIDE-indoor [6], Li *et al.*'s dataset [5], Zhang *et al.*'s dataset [25], and D-Hazy [24] only

TABLE III
RESULTS OF REALNESS EVALUATION OF SYNTHETIC FOGGY IMAGES

Dataset name	AuthESI
FRIDA+ [12], [23]	2.467
Foggy Cityscapes [13]	3.314
RESIDE-outdoor [6]	3.344
O-HAZE [27]	3.819
Dense-Haze [28]	2.749
NH-Haze [29]	3.297
AVID-fog	**2.124**

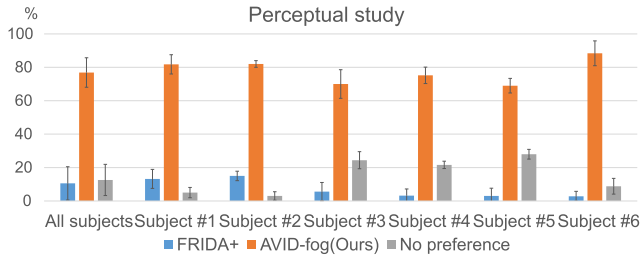

Fig. 7. Results of perceptual realness comparison between AVID and FRIDA+. Seven histograms for individual subjects or all subjects are given. In each histogram, the averages and variances of percentages for different preferences are displayed in three columns.

comprise indoor scenes. However, it is almost impossible to have fog in ordinary indoor scenes in the real physical world. As shown in Fig. 5(c), (d), (f) and (g), foggy indoor scenes violate human's visual cognition, and they would be easily judged as unrealistic. Fig. 5(a) and (b) are selected from FRIDA [12] and FRIDA2 [23], respectively. It can be seen that the synthesized results are not photo-realistic. Fig. 5(e) is a sample selected from NH-Haze [29]. The artificial fog in Fig. 5(e), that is, the vapor produced by fog/haze machines, covers a much smaller area than the area covered by natural fog. By contrast, the synthetic result in Fig. 5(h) is realistic-looking where the scene is more natural, and the distribution of fog is consistent with the change of scene depth.

In Foggy Cityscapes [13] and RESIDE-outdoor [6], the quality of depth maps cannot be guaranteed and consequently the reality of their synthesized foggy scenes is not reliable. Such a fact is demonstrated in Fig. 6. Fig. 6(a) and (d) are clear images selected from foggy Cityscapes and RESIDE-outdoor, respectively. Fig. 6(b) is Fig. 6(a)'s depth map obtained by using a depth map completion algorithm. Fig. 6(e) is Fig. 6(d)'s depth map obtained by using a "depth map from a single-image" method [34]. Apparent errors can be observed on Fig. 6(b) and (e), leading to weird simulation results as shown in Fig. 6(c) and (f).

To objectively evaluate the realness of synthetic foggy images, we adopt the Authenticity Evaluator for Synthetic foggy/hazy Images (AuthESI for short) proposed in [55]. AuthESI is based on constructing a collection of typical natural scene statistic (NSS) features of fog/haze and fitting them to a multivariate Gaussian (MVG) model. The realness of the synthetic image is expressed as the modified Bhattacharyya distance between the natural MVG model and the simulated image's MVG model. A smaller distance means that the simulated image is more natural-looking. In order to show the efficacy of our simulation model, we compared our results with relevant outdoor datasets, including FRIDA/FRIDA2 [12], [23], Foggy Cityscapes [13], RESIDE-outdoor [6], O-HAZE [27], Dense-Haze [28] and NH-Haze [29]. Since FRIDA and FRIDA2 were established following the same strategy and both are small in scale, we combined them as "FRIDA+", including 336 foggy images. In addition, as the competing datasets only contain foggy (homogeneous and heterogeneous) scenes, to be fair and to make the results interpretable, we only used foggy images in AVID in this experiment and denote the set containing them by "AVID-fog". We used the model pre-trained on 180 real foggy and hazy images in [55], and sample 100 images from each dataset for testing. If the number of images in the dataset is less than 100, we used all the data.

The quantitative results are presented in Table III. Experimental results show that AVID-fog achieved the lowest AuthESI value, which means that its NSS features are closest to natural fog/haze. The inaccurate depth maps used by Foggy Cityscapes [13] and RESIDE-outdoor [6] make the fog part of their real-world images not authentic enough. O-HAZE [27], Dense-Haze [28] and NH-Haze [29] all introduce artificial fog into the scene by physical means. The spatial distribution of the artificial fog in O-HAZE [27] and NH-Haze [29] is unnaturally uneven, accounts for their lower AuthESI value. The overall fog density in the Dense-Haze [28] is higher, and its visibility is lower, which may cause its foggy patches to be closer to the real dense fog image. Among the relevant datasets, FRIDA+ has the closest configurations to AVID. Their scenes are outdoor. They have accurate depth maps, and their clear source images are also synthetic. In order to further compare the authenticity of FRIDA+ and AVID, we performed a comprehensive comparison of AVID-fog and FRIDA+ in terms of realness.

Six volunteers were invited in this experiment. For each subject, he/she needed to complete 5 batches of tests. For each batch, we randomly selected 100 samples from FRIDA+ and 100 samples from AVID-fog. Then, the images were shown in pair to the subject. For each pairwise comparison, the subject had three options: "left is more realistic", "right is more realistic", and "no preference". To avoid the subjective bias, the order of pairs and the placement of left and right images within each pair are randomized and are unknown to subjects. The results of this perceptual study are summarized in graphs shown in Fig. 7 where there are seven histograms for individual subjects or all subjects. In each histogram, the averages and variances of percentages for different preferences are displayed in three columns. The participants showed a strong bias in preference towards synthetic results in AVID. Specially, the histogram summarizing preferences of all subjects indicates that: 1) AVID-fog is preferred at the rate of 76.9%; b) FRIDA+ is preferred at the rate of 10.53%; and 3) no preference is selected at the rate of 12.57%. Therefore, we can reach the conclusion that AVID-fog is more realistic than FRIDA+.

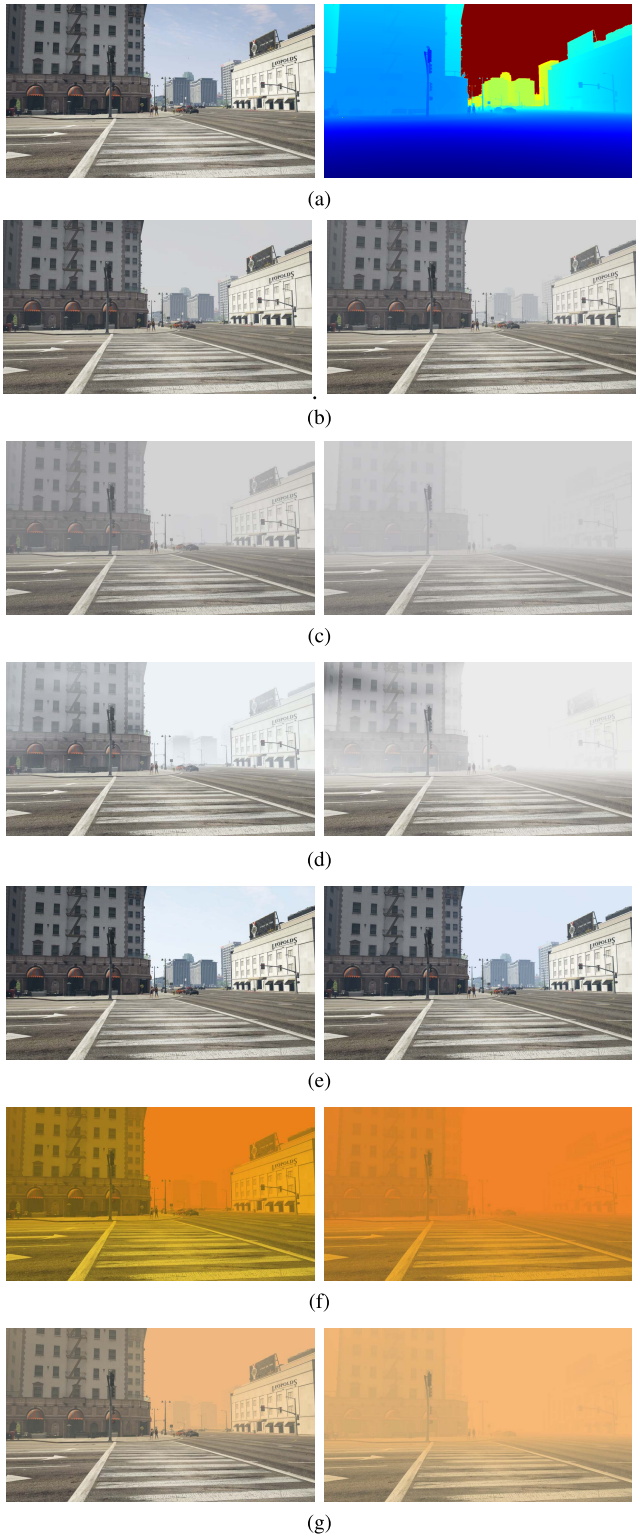

Fig. 8. The left image of (a) is a clear source image while the right one is its depth map. Based on (a), scenes with mist, homogeneous fog, heterogeneous fog, natural haze, smog, and Asian dust are synthesized and the results are shown as (b) ∼ (g), respectively. For each row of (b) ∼ (g), the left image has a larger visibility than the right one.

To facilitate readers to visually examine the realness of images in AVID, synthesized results from a selected clear scene are shown in Fig. 8. The left image of Fig. 8(a) is a clear source image while the right one is its depth map. Based on Fig. 8(a), scenes with mist, homogeneous fog, heterogeneous fog, natural haze, smog, and Asian dust are synthesized and the results are shown as Figs. 8(b) ∼ (g), respectively. For each row of Figs. 8(b) ∼ (g), the left image has a larger visibility than the right one. It can be seen that images synthesized using the proposed schemes are quite realistic.

VI. Conclusion

In the era of deep learning, atmospheric visibility impairment simulation is an issue worthy of deep study. The reason is that it can provide a large amount of data to train vision algorithms that take visibility degradation into account. However, this research direction has not attracted much attention from researchers. In this paper, we first analyzed the limitations and irrationalities of the relevant studies. Then, based on knowledge from the atmospheric science, we proposed approaches to simulate five most commonly seen visibility impairment phenomena, including mist, fog, natural haze, smog, and Asian dust. Using the proposed methods, a large-scale synthetic image dataset AVID was constructed, which contains 40,000 clear source images along with 800,000 visibility-impaired versions. In near future, we will attempt to make use of AVID to develop algorithms for restoring images with atmospheric visibility impairment and algorithms of image-based visibility estimation.

Appendix A
Derivation for Eq. 15

For the smog case, the three terms $b_{scat}(\lambda)$, $b_{abs-gas}(\lambda)$, and $b_{abs-aero}(\lambda)$ of the extinction coefficient $b(\lambda)$ are given as Eqs. 11, 12, 13 in the paper. Then, for the red light, green light, and blue light, the corresponding extinction coefficients b^R, b^G, b^B can be expressed as,

$$\begin{cases} b^R = C_1 \cdot 645.2^{-\alpha} + C_2 \cdot 645.2^{-4} + C_3 \cdot 645.2^{-\beta} \\ b^G = C_1 \cdot 526.3^{-\alpha} + C_2 \cdot 526.3^{-4} + C_3 \cdot 526.3^{-\beta} \\ b^B = C_1 \cdot 444.4^{-\alpha} + C_2 \cdot 444.4^{-3} + C_3 \cdot 444.4^{-\beta} \end{cases} \tag{16}$$

We define C^{RG} as,

$$C^{RG} \triangleq \frac{b^R}{b^G} = \frac{C_1 \cdot 645.2^{-\alpha} + C_2 \cdot 645.2^{-4} + C_3 \cdot 645.2^{-\beta}}{C_1 \cdot 526.3^{-\alpha} + C_2 \cdot 526.3^{-4} + C_3 \cdot 526.3^{-\beta}} \tag{17}$$

On the other hand, it can be proved that if $a > 0$, $b > 0$, $c > 0$, $d > 0$, $e > 0$ and $f > 0$, the following inequality holds,

$$\min\left(\frac{a}{b}, \frac{c}{d}, \frac{e}{f}\right) \leq \frac{a+c+e}{b+d+f} \leq \max\left(\frac{a}{b}, \frac{c}{d}, \frac{e}{f}\right) \tag{18}$$

Based on Eq. 18, it can be verified that $\frac{645.2^{-4}}{526.3^{-4}} \leq C^{RG} \leq \frac{645.2^{-1}}{526.3^{-1}}$. We define C^{RB} as,

$$C^{RB} \triangleq \frac{b^R}{b^B} = \frac{C_1 \cdot 645.2^{-\alpha} + C_2 \cdot 645.2^{-4} + C_3 \cdot 645.2^{-\beta}}{C_1 \cdot 444.4^{-\alpha} + C_2 \cdot 444.4^{-3} + C_3 \cdot 444.4^{-\beta}} \tag{19}$$

It can be verified that $\frac{645.2^{-4}}{444.4^{-3}} \leq C^{RB} \leq \frac{645.2^{-1}}{444.4^{-1}}$. We define C^{GB} as,

$$C^{GB} \triangleq \frac{b^G}{b^B} = \frac{C_1 \cdot 526.3^{-\alpha} + C_2 \cdot 526.3^{-4} + C_3 \cdot 526.3^{-\beta}}{C_1 \cdot 444.4^{-\alpha} + C_2 \cdot 444.4^{-3} + C_3 \cdot 444.4^{-\beta}} \tag{20}$$

It can be verified that $\frac{526.3^{-4}}{444.4^{-3}} \leq C^{GB} \leq \frac{526.3^{-1}}{444.4^{-1}}$. From the definitions of C^{RG}, C^{RB}, and C^{GB}, it can be known that,

$$C^{RB} = C^{RG} \cdot C^{GB} \tag{21}$$

Thus, the value range of C^{RB} can be further shrinked as, $C^{RB} \in \left[\frac{645.2^{-4}}{444.4^{-3}}, \frac{645.2^{-1}}{444.4^{-1}}\right] \cap \left[C^{RG}\frac{526.3^{-4}}{444.4^{-3}}, C^{RG}\frac{526.3^{-1}}{444.4^{-1}}\right]$ when C^{RG} is fixed.

When the light absorption is ignored, Duntley's law (Eq. 4 in the paper) actually is equivalent to Koschmieder's law (Eq. 1 in the paper) and we have $L_a(\lambda) = A(\lambda)b(\lambda)$. For smog case, the light absorption should be considered, and thus $L_a(\lambda) < A(\lambda)b(\lambda)$. Or in another form, we have,

$$L_a^R = k^R b^R A^R \tag{22}$$

$$L_a^G = k^G b^G A^G \tag{23}$$

$$L_a^B = k^B b^B A^B \tag{24}$$

where $k^R \in (0, 1)$, $k^G \in (0, 1)$ and $k^B \in (0, 1)$. By collecting many images with smog and fog, we found that k^R is actually very close to 1. Thus, in our implementation, the value range of k^R is shrinked to $k^R \in (0.9, 1)$.

From Eqs. 17, 22, and 23, we can have,

$$C^{RG} = \frac{b^R}{b^G} = \frac{L_a^R / \left(k^R A^R\right)}{L_a^G / \left(k^G A^G\right)} = \frac{L_a^R k^G A^G}{L_a^G k^R A^R} \tag{25}$$

Then, we can have,

$$k^G = C^{RG} \cdot \frac{L_a^G A^R}{L_a^R A^G} \cdot k^R \tag{26}$$

We define $k^{RG} = \frac{L_a^G A^R}{L_a^R A^G}$. Then, we have,

$$k^G = C^{RG} \cdot k^{RG} \cdot k^R \tag{27}$$

By observing many images with smog and fog, we found that the value range of k^G is very close to that of C^{RG}. So, we assume that $k^{RG}k^R$ is around 1.0. In our implementation, we set $0.8 < k^{RG}k^R < 1.2$. Thus, if k^R is fixed, $k^{RG} \in \left(\frac{0.8}{k^R}, \frac{1.2}{k^R}\right)$.

From Eqs. 19, 22, and 24, we can have

$$C^{RB} = \frac{b^R}{b^B} = \frac{L_a^R / \left(k^R A^R\right)}{L_a^B / \left(k^B A^B\right)} = \frac{L_a^R k^B A^B}{L_a^B k^R A^R} \tag{28}$$

Then, we can have

$$k^B = C^{RB} \cdot \frac{L_a^B A^R}{L_a^R A^B} \cdot k^R \tag{29}$$

We define $k^{RB} = \frac{L_a^B A^R}{L_a^R A^B}$. Then we have,

$$k^B = C^{RB} \cdot k^{RB} \cdot k^R \tag{30}$$

By observing many images with smog and fog, we found that the value range of k^B is very close to that of C^{RB}. So, we assume that $k^{RB}k^R$ is around 1.0. In our implementation, we set $0.8 < k^{RB}k^R < 1.2$. Thus, if k^R is fixed, $k^{RB} \in \left(\frac{0.8}{k^R}, \frac{1.2}{k^R}\right)$.

From Eqs. 17, 23, and 27, we can have

$$L_a^G = b^G k^G A^G = b^G C^{RG} k^{RG} k^R A^G = k^R k^{RG} b^R A^G \tag{31}$$

From Eqs. 19, 24, and 30, we can have,

$$L_a^B = b^B k^B A^B = b^B C^{RB} k^{RB} k^R A^B = k^R k^{RB} b^R A^B \tag{32}$$

The wavelength of the green light is close to 550nm. Therefore, according to Eq. 3 in the paper, when the visibility υ is given, b^G can be roughly computed as,

$$b^G = \frac{-\ln 0.05}{\upsilon} \tag{33}$$

Putting Eqs. 22, 31, 32, 33, 17, and 19 together, we can get Eq. 15 in the paper as,

$$\begin{cases} L_a^R = k^R b^R A^R \\ L_a^G = k^R k^{RG} b^R A^G \\ L_a^B = k^R k^{RB} b^R A^B \\ b^G = \dfrac{-\ln 0.05}{\upsilon} \\ b^R = C^{RG} b^G \\ b^B = \dfrac{b^R}{C^{RB}} \end{cases} \tag{34}$$

APPENDIX B
DERIVATIONS OF VALUE RANGES OF C^{RG} AND C^{RB} FOR SYNTHESIZING ASIAN DUST

The scheme for Asian dust simulation is quite similar to that for smog. The only difference is that for Asian dust $b_{abs-gas}(\lambda)$ can be neglected and thus $b(\lambda) = b_{scat}(\lambda) + b_{abs-aero}(\lambda)$. Then, for the red light, green light, and blue light, the corresponding extinction coefficients b^R, b^G, b^B can be expressed as,

$$\begin{cases} b^R = C_1 \cdot 645.2^{-\alpha} + C_3 \cdot 645.2^{-\beta} \\ b^G = C_1 \cdot 526.3^{-\alpha} + C_3 \cdot 526.3^{-\beta} \\ b^B = C_1 \cdot 444.4^{-\alpha} + C_3 \cdot 444.4^{-\beta} \end{cases} \tag{35}$$

In this case, C^{RG} is,

$$C^{RG} \triangleq \frac{b^R}{b^G} = \frac{C_1 \cdot 645.2^{-\alpha} + C_3 \cdot 645.2^{-\beta}}{C_1 \cdot 526.3^{-\alpha} + C_3 \cdot 526.3^{-\beta}} \tag{36}$$

It can be verified that $\frac{645.2^{-2.3}}{526.3^{-2.3}} \leq C^{RG} \leq \frac{645.2^{-1}}{526.3^{-1}}$. C^{RB} is,

$$C^{RB} \triangleq \frac{b^R}{b^B} = \frac{C_1 \cdot 645.2^{-\alpha} + C_3 \cdot 645.2^{-\beta}}{C_1 \cdot 444.4^{-\alpha} + C_3 \cdot 444.4^{-\beta}} \tag{37}$$

It can be verified that $\frac{645.2^{-2.3}}{444.4^{-2.3}} \leq C^{RB} \leq \frac{645.2^{-1}}{444.4^{-1}}$. C^{GB} is,

$$C^{GB} \triangleq \frac{b^G}{b^B} = \frac{C_1 \cdot 526.3^{-\alpha} + C_3 \cdot 526.3^{-\beta}}{C_1 \cdot 444.4^{-\alpha} + C_3 \cdot 444.4^{-\beta}} \tag{38}$$

It can be verified that $\frac{526.3^{-2.3}}{444.4^{-2.3}} \leq C^{GB} \leq \frac{526.3^{-1}}{444.4^{-1}}$. Since $C^{RB} = C^{RG} \cdot C^{GB}$, the value range of C^{RB} can be further shrinked as,

$$C^{RB} \in \left[\frac{645.2^{-2.3}}{444.4^{-2.3}}, \frac{645.2^{-1}}{444.4^{-1}}\right] \cap \left[C^{RG}\frac{526.3^{-2.3}}{444.4^{-2.3}}, C^{RG}\frac{526.3^{-1}}{444.4^{-1}}\right] \quad (39)$$

when C^{RG} is fixed.

REFERENCES

[1] N. Buch, S. A. Velastin, and J. Orwell, "A review of computer vision techniques for the analysis of urban traffic," *IEEE Trans. Intell. Transp. Syst.*, vol. 12, no. 3, pp. 920–939, Mar. 2011.

[2] D. Dai and W. Yang, "Satellite image classification via two-layer sparse coding with biased image representation," *IEEE Geosci. Remote Sens. Lett.*, vol. 8, no. 1, pp. 173–176, Aug. 2011.

[3] L. Zhang, J. Huang, X. Li, and L. Xiong, "Vision-based parking-slot detection: A DCNN-based approach and a large-scale benchmark dataset," *IEEE Trans. Image Process.*, vol. 27, no. 11, pp. 5350–5364, Nov. 2018.

[4] K. He, J. Sun, and X. Tang, "Single image haze removal using dark channel prior," *IEEE Trans. Pattern. Anal. Mach. Intell.*, vol. 33, no. 12, pp. 2341–2353, Sep. 2011.

[5] B. Li, X. Peng, Z. Wang, J. Xu, and D. Feng, "AOD-Net: All-in-one dehazing network," in *Proc. IEEE Int. Conf. Comput. Vis. (ICCV)*, Oct. 2017, pp. 4780–4788.

[6] B. Li *et al.*, "Benchmarking single-image dehazing and beyond," *IEEE Trans. Image Process.*, vol. 28, no. 1, pp. 492–505, Jan. 2019.

[7] R. Li, J. Pan, Z. Li, and J. Tang, "Single image dehazing via conditional generative adversarial network," in *Proc. IEEE/CVF Conf. Comput. Vis. Pattern Recognit.*, Jun. 2018, pp. 8202–8211.

[8] W. Ren *et al.*, "Gated fusion network for single image dehazing," in *Proc. IEEE/CVF Conf. Comput. Vis. Pattern Recognit.*, Jun. 2018, pp. 3253–3261.

[9] W. Ren, H. Zhang, S. Liu, J. Pan, X. Cao, and M. Yang, "Single image dehazing via multi-scale convolutional neural networks," in *Proc. Eur. Conf. Comput. Vis.*, 2016, pp. 154–169.

[10] M. Ju, C. Ding, W. Ren, Y. Yang, D. Zhang, and Y. J. Guo, "IDE: Image dehazing and exposure using an enhanced atmospheric scattering model," *IEEE Trans. Image Process.*, vol. 30, pp. 2180–2192, 2021.

[11] M. Ju, C. Ding, Y. J. Guo, and D. Zhang, "IDGCP: Image dehazing based on gamma correction prior," *IEEE Trans. Image Process.*, vol. 29, pp. 3104–3118, 2020.

[12] J.-P. Tarel, N. Hautiere, A. Cord, D. Gruyer, and H. Halmaoui, "Improved visibility of road scene images under heterogeneous fog," in *Proc. IEEE Intell. Vehicles Symp.*, Jun. 2010, pp. 478–485.

[13] C. Sakaridis, D. Dai, and L. Van Gool, "Semantic foggy scene understanding with synthetic data," *Int. J. Comput. Vis.*, vol. 126, no. 9, pp. 973–992, 2018.

[14] Y. You, C. Lu, W. Wang, and C.-K. Tang, "Relative CNN-RNN: Learning relative atmospheric visibility from images," *IEEE Trans. Image Process.*, vol. 28, no. 1, pp. 45–55, Jan. 2019.

[15] M. Johnson-Roberson, C. Barto, R. Mehta, S. N. Sridhar, K. Rosaen, and R. Vasudevan, "Driving in the matrix: Can virtual worlds replace human-generated annotations for real world tasks?" in *Proc. IEEE Int. Conf. Robot. Automat. (ICRA)*, May 2017, pp. 746–753.

[16] G. Ros, L. Sellart, J. Materzynska, D. Vazquez, and A. M. Lopez, "The SYNTHIA dataset: A large collection of synthetic images for semantic segmentation of urban scenes," in *Proc. IEEE Conf. Comput. Vis. Pattern Recognit. (CVPR)*, Jun. 2016, pp. 3234–3243.

[17] A. Gaidon, Q. Wang, Y. Cabon, and E. Vig, "Virtual worlds as proxy for multi-object tracking analysis," in *Proc. IEEE Conf. Comput. Vis. Pattern Recognit. (CVPR)* Jun. 2016, pp. 4340–4349.

[18] M. Müller, V. Casser, J. Lahoud, N. Smith, and B. Ghanem, "Sim4CV: A photo-realistic simulator for computer vision applications," *Int. J. Comput. Vis.*, vol. 126, no. 9, pp. 902–919, Sep. 2018.

[19] A. Dosovitskiy, G. Ros, F. Codevilla, A. Lopez, and V. Koltun, "CARLA: An open urban driving simulator," in *Proc. 1st Annu. Conf. Robot Learn.*, vol. 78, 2017, pp. 1–16.

[20] S. R. Richter, Z. Hayder, and V. Koltun, "Playing for benchmarks," in *Proc. IEEE Int. Conf. Comput. Vis. (ICCV)*, Oct. 2017, pp. 2232–2241.

[21] M. Angus *et al.*, "Unlimited road-scene synthetic annotation (URSA) dataset," in *Proc. 21st Int. Conf. Intell. Transp. Syst. (ITSC)*, Nov. 2018, pp. 985–992.

[22] S. R. Richter, V. Vineet, S. Roth, and V. Koltun, "Playing for data: Ground truth from computer games," in *Proc. Eur. Conf. Comput. Vis.*, 2016, pp. 102–118.

[23] J. P. Tarel, N. Hautiere, L. Caraffa, A. Cord, H. Halmaoui, and D. Gruyer, "Vision enhancement in homogeneous and heterogeneous fog," *IEEE Intell. Transp. Syst. Mag.*, vol. 4, no. 2, pp. 6–20, Apr. 2012.

[24] C. Ancuti, C. O. Ancuti, and C. De Vleeschouwer, "D-HAZY: A dataset to evaluate quantitatively dehazing algorithms," in *Proc. IEEE Int. Conf. Image Process. (ICIP)*, Sep. 2016, pp. 2226–2230.

[25] H. Zhang and V. M. Patel, "Densely connected pyramid dehazing network," in *Proc. IEEE/CVF Conf. Comput. Vis. Pattern Recognit.*, Jun. 2018, pp. 3194–3203.

[26] C. Ancuti, C. O. Ancuti, R. Timofte, and C. De Vleeschouwer, "I-HAZE: A dehazing benchmark with real hazy and haze-free outdoor images," in *Proc. Int. Conf. Adv. Concepts Intell. Vis. Syst.* Cham, Switzerland: Springer, Sep. 2018, pp. 620–631.

[27] C. O. Ancuti, C. Ancuti, R. Timofte, and C. De Vleeschouwer, "O-HAZE: A dehazing benchmark with real hazy and haze-free outdoor images," in *Proc. IEEE/CVF Conf. Comput. Vis. Pattern Recognit. Workshops (CVPRW)*, Jun. 2018, pp. 754–762.

[28] C. O. Ancuti, C. Ancuti, M. Sbert, and R. Timofte, "Dense-Haze: A benchmark for image dehazing with dense-haze and haze-free images," in *Proc. IEEE Int. Conf. Image Process. (ICIP)*, Sep. 2019, pp. 1014–1018.

[29] C. O. Ancuti, C. Ancuti, and R. Timofte, "NH-HAZE: An image dehazing benchmark with non-homogeneous hazy and haze-free images," in *Proc. IEEE/CVF Conf. Comput. Vis. Pattern Recognit. Workshops (CVPRW)*, Jun. 2020, pp. 444–445.

[30] W. E. K. Middleton, "Vision through the atmosphere," in *Geophysik II/Geophysics II*, J. Bartels, Ed. Berlin, Germany: Springer, 1957.

[31] M. Cordts *et al.*, "The cityscapes dataset for semantic urban scene understanding," in *Proc. IEEE Conf. Comput. Vis. Pattern Recognit. (CVPR)*, Jun. 2016, pp. 3213–3223.

[32] N. Silberman, D. Hoiem, P. Kohli, and R. Fergus, "Indoor segmentation and support inference from RGBD images," in *Proc. Eur. Conf. Comput. Vis.*, 2012, pp. 746–760.

[33] D. Scharstein and R. Szeliski, "High-accuracy stereo depth maps using structured light," in *Proc. IEEE Comput. Soc. Conf. Comput. Vis. Pattern Recognit.*, Jun. 2013. p. 1.

[34] F. Liu, C. Shen, G. Lin, and I. Reid, "Learning depth from single monocular images using deep convolutional neural fields," *IEEE Trans. Pattern Anal. Mach. Intell.*, vol. 38, no. 10, pp. 2024–2039, Oct. 2016.

[35] S. Song, S. P. Lichtenberg, and J. Xiao, "SUN RGB-D: A RGB-D scene understanding benchmark suite," in *Proc. IEEE Conf. Comput. Vis. Pattern Recognit. (CVPR)*, Jun. 2015, pp. 567–576.

[36] A. Saxena, M. Sun, and A. Y. Ng, "Make3D: Learning 3D scene structure from a single still image," *IEEE Trans. Pattern Anal. Mach. Intell.*, vol. 31, no. 5, pp. 824–840, May 2009.

[37] S. Q. Duntley, "The reduction of apparent contrast by the atmosphere," *J. Opt. Soc. Amer.*, vol. 38, no. 2, pp. 179–191, 1948.

[38] R. J. Charlson, "Atmospheric visibility related to aerosol mass concentration: Review," *Environ. Sci. Technol.*, vol. 3, no. 10, pp. 913–918, Oct. 1969.

[39] J. B. Farrow and A. F. Gibson, "Influence of the atmosphere on optical systems," *Opt. Acta, Int. J. Opt.*, vol. 17, no. 5, pp. 317–336, May 1970.

[40] *Grade of Fog Forecast*, Standards GB/T 27964-2011, National Standards of People's Republic of China, 2011.

[41] K. Perlin, "Improving noise," *ACM Trans. Graph.*, vol. 21, no. 3, pp. 681–682, 2002.

[42] L.-H. Guo, "Haze and health," *Nat. Sci. Rev.*, vol. 3, no. 4, pp. 412–413, Dec. 2016.

[43] R. Zhang *et al.*, "Formation of nanoparticles of blue haze enhanced by anthropogenic pollution," *Proc. Nat. Acad. Sci. USA*, vol. 106, no. 42, pp. 17650–17654, 2009.

[44] C. Oleari, *Standard Colorimetry: Definitions, Algorithms and Software*. Hoboken, NJ, USA: Wiley, 2016.

[45] R. S. Cowan, *A Social History of American Technology*. Oxford, U.K.: Oxford Univ. Press, 1997.

[46] R. B. Husar and W. H. White, "On the color of the Los Angeles SMOG," *Atmos. Environ.*, vol. 10, no. 3, pp. 199–204, Jan. 1976.

[47] R. J. Charlson, D. S. Covert, Y. Tokiwa, and P. K. Mueller, "Multi-wavelength nephelometer measurements in Los Angeles smog aerosol," *J. Colloid Interface Sci.*, vol. 39, no. 1, pp. 260–265, 1972.
[48] T. W. Kirchstetter, T. Novakov, and P. V. Hobbs, "Evidence that the spectral dependence of light absorption by aerosols is affected by organic carbon," *J. Geophys. Res., Atmos.*, vol. 109, no. D21, pp. 1–12, Nov. 2004.
[49] R. W. Bergstrom, P. B. Russell, and P. Hignett, "Wavelength dependence of the absorption of black carbon particles: Predictions and results from the TARFOX experiment and implications for the aerosol single scattering albedo," *J. Atmos. Sci.*, vol. 59, no. 3, pp. 567–577, Feb. 2002.
[50] I. N. Sokolik and O. B. Toon, "Direct radiative forcing by anthropogenic airborne mineral aerosols," *Nature*, vol. 381, no. 6584, pp. 681–683, Jun. 1996.
[51] R. J. Charlson and N. C. Ahlquist, "Brown haze: NO_2, or aerosol?" *Atmos. Environ.*, vol. 3, no. 6, pp. 653–656, 1969.
[52] N. C. Ahlquist and R. J. Charlson, "Measurement of the wavelength dependence of atmospheric extinction due to scatter," *Atmos. Environ.*, vol. 3, no. 5, pp. 551–564, Sep. 1969.
[53] H. Duff, *Air Quality Monitoring, Assessment and Management*. New York, NY, USA: Scitus Academic, 2016.
[54] C. H. Jung, J. Y. Lee, J. Um, S. S. Lee, and Y. P. Kim, "Chemical composition based aerosol optical properties according to size distribution and mixture types during smog and Asian dust events in Seoul, Korea," *Asia–Pacific J. Atmos. Sci.*, vol. 54, no. 1, pp. 19–32, Feb. 2018.
[55] N. Zhang, L. Zhang, and Z. Cheng, "Towards simulating foggy and hazy images and evaluating their authenticity," in *Proc. Int. Conf. Neural Inf. Process.* New York, NY, USA: Springer, Oct. 2017, pp. 405–415.

Lin Zhang (Senior Member, IEEE) received the B.Sc. and M.Sc. degrees from the Department of Computer Science and Engineering, Shanghai Jiao Tong University, Shanghai, China, in 2003 and 2006, respectively, and the Ph.D. degree from the Department of Computing, The Hong Kong Polytechnic University, Hong Kong, in 2011. From March 2011 to August 2011, he was a Research Associate with the Department of Computing, The Hong Kong Polytechnic University. In August 2011, he joined the School of Software Engineering, Tongji University, Shanghai, where he is currently a Full Professor. His current research interests include environment perception of intelligent vehicle, pattern recognition, computer vision, and perceptual image/video quality assessment. He was awarded as a Young Scholar of Changjiang Scholars Program, Ministry of Education, China. He serves as an Associate Editor for IEEE ROBOTICS AND AUTOMATION LETTERS and *Journal of Visual Communication and Image Representation*.

Anqi Zhu received the B.S. degree from the School of Software Engineering, Tongji University, Shanghai, China, in 2019, where she is currently pursuing the master's degree. Her research interests are image restoration, image exposure correction, and machine learning.

Shiyu Zhao received the B.S. degree from the School of Software Engineering, Tongji University, Shanghai, China, in 2017, where he is currently pursuing the master's degree. His research interests are visibility enhancement for bad weather images, scene understanding, and machine learning.

Yicong Zhou (Senior Member, IEEE) received the B.S. degree in electrical engineering from Hunan University, Changsha, China, and the M.S. and Ph.D. degrees in electrical engineering from Tufts University, Medford, MA, USA. He is currently an Associate Professor and the Director of the Vision and Image Processing Laboratory, Department of Computer and Information Science, University of Macau, Macau, China. His research interests include chaotic systems, multimedia security, computer vision, and machine learning. He is a Senior Member of the International Society for Optical Engineering (SPIE). He was a recipient of the Third Price of Macau Natural Science Award in 2014. He is the Co-Chair of the Technical Committee on Cognitive Computing in the IEEE Systems, Man, and Cybernetics Society. He serves as an Associate Editor for *Neurocomputing*, *Journal of Visual Communication and Image Representation*, and *Signal Processing: Image Communication*.